communications materials

A Nature Portfolio journal

Article

https://doi.org/10.1038/s43246-025-00997-8

Molecular dynamics insights into Ti_3C_2 MXene/chitosan composite as a flame-retardant barrier

Ivan Miguel De Cachinho Cordeiro[1,5], Timothy Bo Yuan Chen[2,5], Anthony Chun Yin Yuen[3] ✉, Bo Lin[1], Ming Jia[1], Wei Wang[1], Qian Chen[2], Wen-Jie Yang[2,4], Chang Tian[3], Cheng Wang[1] & Guan Heng Yeoh[1] ✉

Two-dimensional Ti_3C_2 MXenes exhibit remarkable thermal stability and flame resistance, while hybridisation with bio-based chitosan (CS) enhances their effectiveness as flame-proof coating. However, the underlying flame-retardant (FR) mechanisms remain insufficiently resolved at the atomistic scale. Herein, reactive molecular dynamics simulations (MD-ReaxFF) alongside experiments (TGA-FTIR, SEM, XRD, XPS) elucidate the FR pathways of MXene/CS nanosheets. MXene/CS exhibits flame retardancy through three synergistic pathways: (1) releasing organic volatiles to dilute oxidisers; (2) depositing hydroxyl and nitrogen groups to passivate reactive sites; and (3) reinforcing char formation by strengthening C-C and Ti-C bonding. Multilayer MXene/CS coatings exhibit sequential FR behaviour, where sacrificial TiO_2 layers, interlayer carbonisation, and volatile exclusion collectively maintain structural stability under extreme heating. Experimental validation confirms the organic volatiles, enhanced char yield, TiO_2 transformation, and surface functionalisation. These insights establish a mechanistic framework for MXene-based hybrids and highlight CS as a sustainable charring agent, offering design principles for future lightweight and multifunctional flame-retardant coatings.

Polymeric materials are highly combustible and pose significant fire hazards to public safety, as they release intense heat and toxic gases under high-temperature conditions[1]. Utilising carbon-based flame-retardant (FR) coatings to flame-proof polymeric materials represents an effective solution whereby the carbon materials are able to generate a carbonaceous protective layer to protect the material substrates from heat impact and exclude oxidisers to hinder chain reactions[2]. The trade-off between weight gain, flame resistance efficiency, and other material design constraints—such as electrical conductivity and biocompatibility—remains unresolved. This challenge has led researchers to explore solutions through the synthesis of inherently lightweight nanoscale carbon-based coatings.

Among the many advancements in two-dimensional (2D) nanomaterials, metal carbides known as MXenes, discovered in 2011[3], have been extensively studied for their remarkable mechanical, electronic, and optical properties[4]. Their sub-nanometre interlayer gaps between 2D sheets enable fast ion intercalation and transport. Structurally, MXenes are a hexagonal closed-packed (hcp) crystal structure, where the transitional metal sites (i.e. Ti, Mo) were converted to close-packed arrangements, and X (i.e. C, N) atoms are located at octahedral sites between the planes of M atoms. Notably, Ti_3C_2 nanosheets exfoliated from the MAX phase exhibit high thermal and electrical conductivity along with a low thermal expansion coefficient[5]. At elevated temperatures, Ti_3C_2 nanosheets undergo oxidation, transforming into carbon-supported TiO_2 hybrids. During this process, the surface Ti layers oxidise into either rutile or anatase TiO_2, while oxygen diffusion within the structure leads to the release of CO and CO_2. Experimental work has reported that Ti_3C_2 nanosheets are thermally stable up to 1073 K in argon ambient[6], while the transformation of rutile or anatase TiO_2 begins from 470 K and achieves carbon-supported TiO_2 hybrids at 1420 K[7]. As a next-generation material, Ti_3C_2 exhibits exceptional flame-resistant performance in high-temperature environments. During phase transformation, it forms carbon-supported TiO_2 hybrids, which provide effective shielding against heat transfer, smoke generation, and the catalytic

---

[1]School of Mechanical and Manufacturing Engineering, University of New South Wales, Sydney, NSW, Australia. [2]Department of Architecture and Civil Engineering, City University of Hong Kong, Hong Kong, China. [3]Department of Building Energy and Environment Engineering, The Hong Kong Polytechnic University, Hong Kong, China. [4]School of Energy, Materials and Chemical Engineering, Hefei University, Hefei, Anhui, China. [5]These authors contributed equally: Ivan Miguel De Cachinho Cordeiro, Timothy Bo Yuan Chen. ✉e-mail: anthony-cy.yuen@polyu.edu.hk; g.yeoh@unsw.edu.au

attenuation of toxic fumes[8]. MXene nanosheets can also be deposited onto polymer surfaces using layer-by-layer (LbL) assembly. In this methodology, multifunctional bilayers are held together by various attractive forces, including Van der Waals interactions, electrostatic attraction, and hydrogen bonding[9]. This approach enables the precise nano-engineering of FR coatings, allowing for the incorporation of selected additives such as phosphorus-based, nitrogen-based, or other charring agents into the multilayer system. Notably, MXene nanosheets hybridised with chitosan (CS) exhibit remarkable synergistic effects with Ti_3C_2 MXene nanosheets, significantly enhancing char formation and strengthening physical barrier properties for improved flame protection[10,11]. As a polysaccharide derivative of chitin, CS offers remarkable hydrophilicity, biodegradability, and cost-effectiveness. Owing to its hydrophilic groups, CS easily integrates with MXene via solution mixing or LbL approaches[12], enabling the development of MXene/CS layered structures for applications in thermal resistance, electromagnetic interference (EMI) shielding[13], biosensing[4] and water purification[14]. Understanding the synergistic FR mechanism between MXene and CS remains nonetheless challenging due to atomistic and instantaneous interfacial/interlayer reactions, including surface modification and carbon arrangement leading to graphitisation. These phenomena are difficult to observe using conventional microscopy and analytical techniques. Particularly, the fundamental role of CS in reinforcing MXene's thermal resistance at the atomic level remains unexplored, necessitating a dynamic evaluation of the nanomaterial throughout the thermal decomposition and charring process.

Recently, the emergence of computational material science utilising molecular dynamics (MD) simulations has revolutionised the characterisation of next-generation materials, which dynamically extract morphology[15], chemical bonding[16], and other physical properties[17] of MXenes in different pre-defined environments. Specifically, reactive force field molecular dynamics (MD-ReaxFF) is a powerful tool for capturing and analysing the rapid, radical-driven reactions of oxidative thermal decomposition. MD-ReaxFF incorporates interatomic potentials, enabling the consideration of bond formation and dissociation based on bond distances and orders[18]. Early studies using MD-ReaxFF to investigate the oxidation physics of MXene can be found in the model developed by Lotfi et al.[19], where they have fundamentally characterised the thermal oxidation process of Ti_3C_2 slabs in different environments and captured the evolution of carbon arrangements in the carbon-TiO_2 hybrid structures. Meanwhile, Badawy et al.[20] focused on the phase transformation to TiO_2 architectures from MXenes with different surface terminations. Lately, Liu et al.[21] combined aberration-corrected environmental transmission electron microscopy (AC-ETEM) and MD-ReaxFF simulations to explore the crystal plane-dependent oxidation of Ti_3C_2 and expansion owing to coordination and charge differences of superficial Ti atoms. To the best of our knowledge, no published studies have characterised the thermal oxidation of Ti_3C_2 nanosheets, specifically examining their thermal resistance mechanisms and interlayer interactions with FR additives at elevated temperatures. The detailed atomistic reaction between MXenes and CS during flame resistance also remains unexplored, specifically the pyrolysis hindrance CS offers to MXene via surface adsorption and barrier effect.

This study seeks to establish a fundamental understanding of the naturally occurring thermal oxidation of Ti_3C_2 nanosheets under the influence of CS, employing MD-ReaxFF simulations complemented by analytical experiments. A new force field was parameterised using density functional theory (DFT) calculations to enable the oxidation of Ti_3C_2 slabs and their interfacial interactions with CS. These simulations provide valuable insights and enable a dynamic evaluation of MXene and MXene/CS's thermal resistance chemistry across various orientations and layering scenarios. This includes the transformation of carbon-supported TiO_2, the carbonisation of amorphous char, and gas-phase diffusion. The elucidated microscopic information, including gas species spectrum, crystallinity and residue composition of the MXene simulations, is benchmarked against several analytical experiments (i.e. XPS, XRD and TG-FTIR) to probe the flame-retardant pathway of MXene/CS interlayers.

Results and discussion

Evolution of MXene surface oxidation

To elucidate the intrinsic oxidation chemistry of pristine MXene slabs with the newly trained ReaxFF potentials, a series of MD simulations on Ti_3C_2 nanosheets were performed at 2000 K, 2500 K, and 3000 K. Figure 1(a) illustrates the transient evolution of single-slab Ti_3C_2 oxidation at 3000 K from 0 to 300 ps (see Supplementary Movie 1). The thermal oxidation of MXene is initiated by oxygen diffusion surrounding the slab, which facilitates an irreversible phase transformation, leading to the formation of amorphous carbon-supported TiO_2 hybrids as temperature increases.

Figure 1(b) further illustrates the lattice and atomic-scale reconfiguration, highlighting the transition of the carbon layer from a crystalline to an amorphous state due to Ti–C bond dissociation. Concurrently, the Ti layer undergoes rapid oxidation, resulting in its conversion into tetragonal rutile or anatase TiO_2.

To probe the atomic reconfiguration, Fig. 1(c) depicts the Radial distribution function (RDF) spectrum of the MXene, which reveals the averaged interatomic distances. During oxidation, the Ti-Ti distance reduced from 3.1 Å to 2.7 Å noticeably owing to the formation of the Ti-O-Ti and O-Ti-O bond during TiO_2 transformation. Simultaneously, the weakening of Ti-C interactions significantly accelerates Ti-C bond dissociation, resulting in diminished peak intensity for Ti-C as oxidation progresses. The residual carbon fragments agglomerate to chain-like carbon in an amorphous state under high temperatures via compact C-C bonding (~1.2 Å).

Figure 1(d) quantifies the gases detected during oxidation at 2000 K, 2500 K and 3000 K, demonstrating that CO and CO_2 constitute the predominant volatiles from the oxidation of $Ti_3C_2O_2$. The findings suggest that oxygen diffusion through surface openings induces a β-scission reaction on local carbon chains, leading to CO and CO_2 release. In comparison, the oxidation dynamics are most aggressive, yielding 73 CO and 20 CO_2 molecules after 300 ps. Although the gasification rates at 2000 K and 2500 K were relatively slow due to limited energy availability and reaction timescales, oxygen consumption remains remarkably consistent across the cases. This can be attributed to the reaction phases of 2000 K and 2500 K, where oxidation of the surface Ti layer precedes substantial carbon gasification. Additionally, oxidation product volatiles can be further characterised via the TGA-FTIR experiment.

Figure 2 (a) presents the FTIR spectrum of MXene at different temperatures during TGA analysis in an oxygen environment. A significant CO_2 pattern is identified after the temperature increased over 350 °C, where the asymmetric stretch (2363.52 cm^{-1} and 2330.64 cm^{-1}), symmetric stretch (1584.59 cm^{-1}) and bending vibration (670 cm^{-1}) of CO_2 were detected. The results obtained from MD simulations strongly support the postulated thermal oxidation reaction of MXene:

$$Ti_3C_2O_2 + 4O_2 = 3TiO_2 + CO_2 + Amorphous\ C$$

This thermally driven reaction aligns with previous experimental and numerical studies[7–9,19], beginning with the transformation of the surface Ti layer into rutile or anatase TiO_2 via oxidation. The hybrid layers exhibit excellent flame-resistant properties, maintaining structural stability under extreme heat (3000 K) due to compact C-C and Ti-Ti interatomic distances that dissipate heat and restrain further oxidation. However, once the surface Ti layer completes its phase transformation, residual carbon remains susceptible to oxidation. Oxygen diffusion through surface openings enables the oxidation of carbon chains, leading to further degradation. SEM images of MXene before and after TGA further illustrate its thermal oxidative behaviour.

Figure 2(b), (d) capture the surface morphology of MXene slabs pre-TGA at magnifications of 1 μm and 0.5 μm, confirming the fabrication of Ti_3C_2 nanosheets with lateral dimensions of ~0.5 μm and ultrathin thickness. The flake-like pattern remained intact, with no noticeable defects. Post-TGA analysis (Fig. 2(c), (e)) reveals a significant transformation into rutile- and anatase-like TiO_2 structures, which dominate the images,

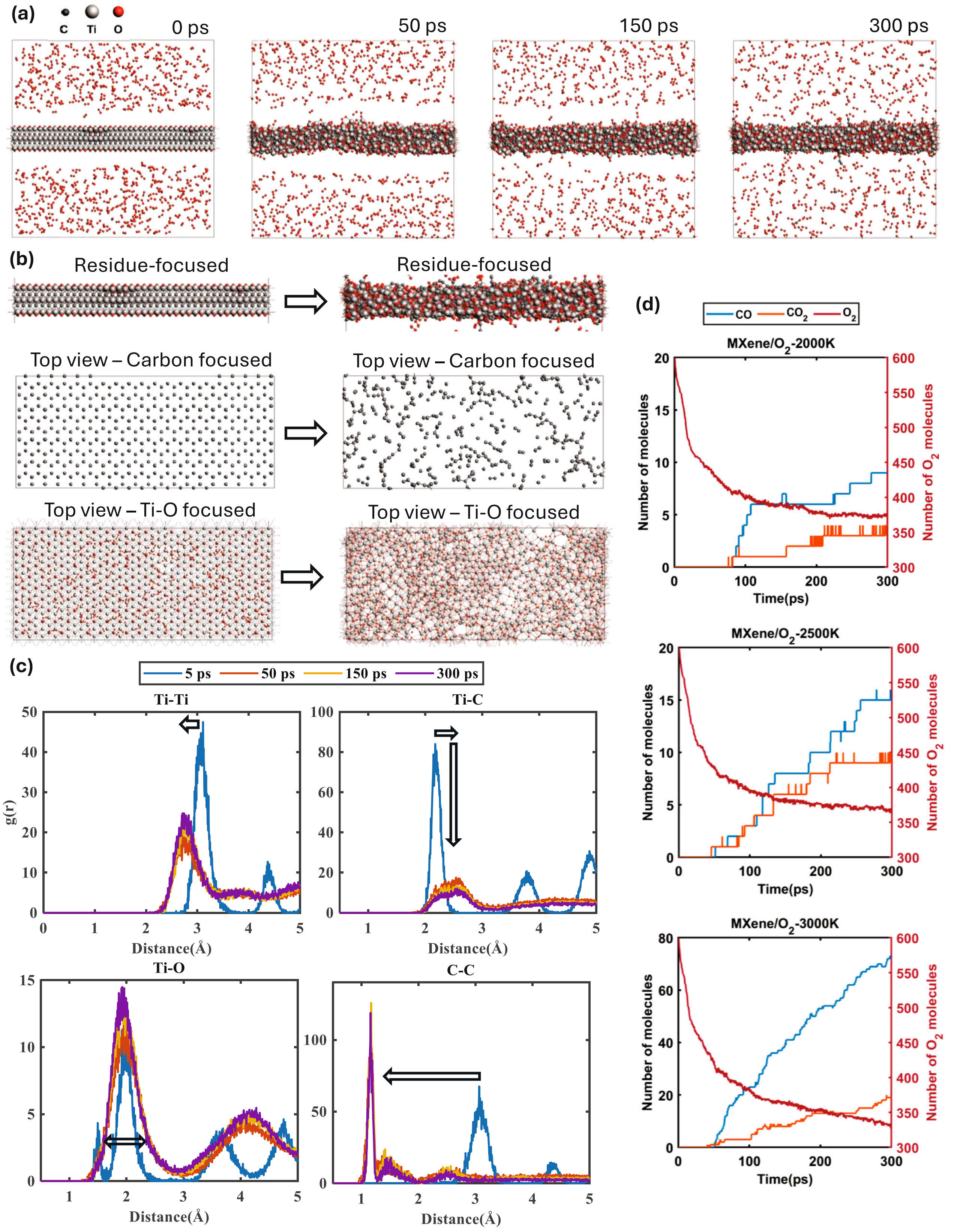

Fig. 1 | MD simulations of pristine MXene oxidation. a Snapshots of MXene/O_2 at 3000 K; **b** Snapshots of lattice at 3000 K, with displaying carbon or Titanium, oxygen only; **c** RDF spectra of MXene at 3000 K; **d** Product distribution of MXene/O_2 at different temperatures.

indicating that TiO_2 constitutes the primary or majority oxidation product at high temperatures.

The TiO_2 transformation of MXene can be further studied using X-ray photoelectron spectroscopy (XPS). Figure 2(f) reveals the high-resolution Ti2p spectrum of MXene before TG. It demonstrates several distinct peaks at 455, 456.5, 457.5, 459.5, 461 and 465.5 eV, which correspond to Ti-C, Ti(II), Ti(III), Ti(IV)-TiO_2, $TiO_{2-x}F_{2x}$, and C-Ti-F assignments respectively[22]. This confirms the intact Ti_3C_2 structure consisting of a Ti-C network in the interior MXene

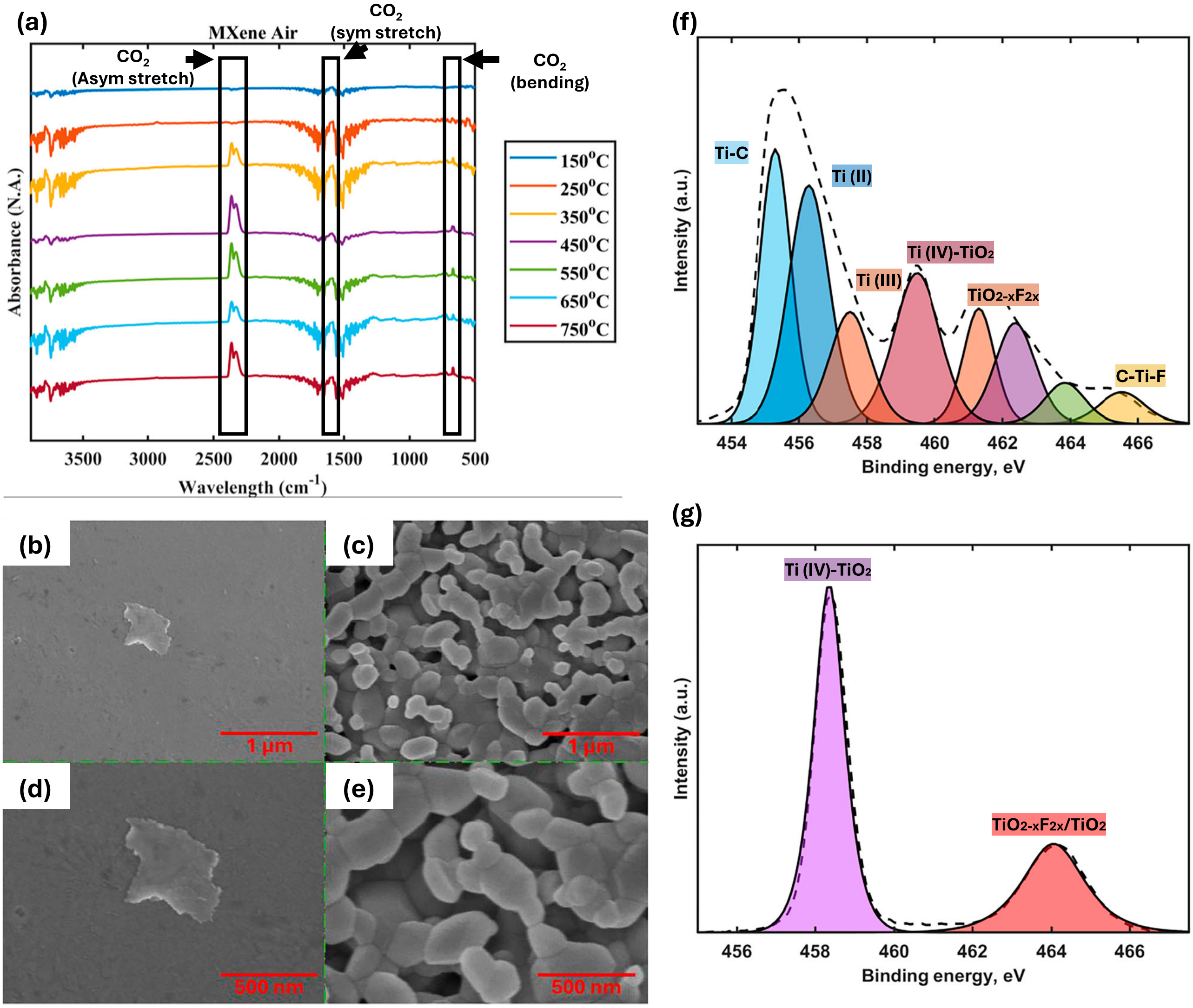

Fig. 2 | Experimental confirmation of pristine MXene oxidation. **a** TGA-FTIR spectrum of MXene an oxygen environment; SEM images of the MXene sample at 1 µm (**b**) before TGA; **c** After TGA (N_2); at 0.5 µm **d** before TGA; **e** After TGA (N_2); XPS Ti2p spectrum of MXene **f** before TGA; **g** After TGA.

layers, with partial surface oxidation that forms mixed oxides (TiO_xF_y) and carboxides (TiC_xO_y). However, distinct peaks indicating oxidation can be identified in the high-resolution Ti2p spectrum of MXene after TG in Fig. 2(g), where sharp TiO_2 signals at 458.6 eV and $TiO_{2-x}F_{2x}/TiO_2$ at 464 eV[23] indicate the complete TiO_2 transformation during oxidation. The detailed XPS analysis on MXene before and after TG can be found in Supplementary Fig. 3 and Supplementary Fig. 4.

Influence of CS on MXene thermal decomposition

During the hybridisation between MXene and CS, the interfacial/interlayer reactions—comprising surface modification and graphitisation—occur instantaneously at the molecular scale, making them extremely difficult to observe using conventional microscopy or analytical techniques. In this section, the influence of CS on MXene's thermal decomposition can be investigated by introducing CS chains into the free periodic domain in both oxygen and vacuum environments in MD simulations, as shown in Fig. 3(a), (b) (see Supplementary Movie 2 and Supplementary Movie 3). Both systems were heated at 3000 K, triggering rapid degradation of CS upon the initiation of heating. During decomposition, d-glucosamine chains are broken down into low-molecular-weight fragments (e.g. H_2O, NH_3, H_2, C_2H_2O, etc.) along with other aliphatic carbon residues.

Figure 3(c) compares the number of major volatiles released in oxygen and vacuum environments. Owing to the high nitrogen and hydroxyl content in CS, significant amounts of organic molecules such as H_2O and NH_3 were emitted during decomposition. These gaseous species are commonly detected in FR systems, where they help to dilute the surrounding combustible gases and oxidisers in flaming scenarios[1,24]. Notably, the MXene/CS system released more NH_3 and H_2 in the absence of oxygen, nearly twice the NH_3 compared to the oxidation scenario, indicating more excellent FR activity in the gas phase.

Gaseous species that were detected also agreed with the TGA-FTIR results. Figure 3(d) reveals the TGA-FTIR spectrum of MXene/CS at different temperatures in nitrogen. At early thermal behaviour, strong and broad vibration peaks can be observed at ~3700–3500 cm^{-1} and ~1500–1700 cm^{-1}, which correspond to typical O-H stretch and H-O-H bending of water vapour, indicating evaporation from the samples at 150 °C and 250 °C. Beyond 250 °C, sharp peaks at 2363.52 cm^{-1}, 2330.64 cm^{-1} and 670 cm^{-1} progressively emerge, closely resembling the CO_2 pattern discovered in pure MXene oxidation FTIR spectrum (see Fig. 2(a)). The emission of CO_2 can be attributed to both the oxidation of MXene and the decarboxylation of CS. Most significantly, a series of characteristic peaks persists beyond 450 °C, which can be identified as the following potential species:

(1) *Cyanoacetic acid/acetic acid-based*: sharp peaks were observed at 1120.1 cm^{-1} (C–N stretching in nitrile (–CN) group), 1280 cm^{-1} and 1300 cm^{-1} (C–O stretching in carboxyl (-COOH) group)[25], 1800 cm^{-1}

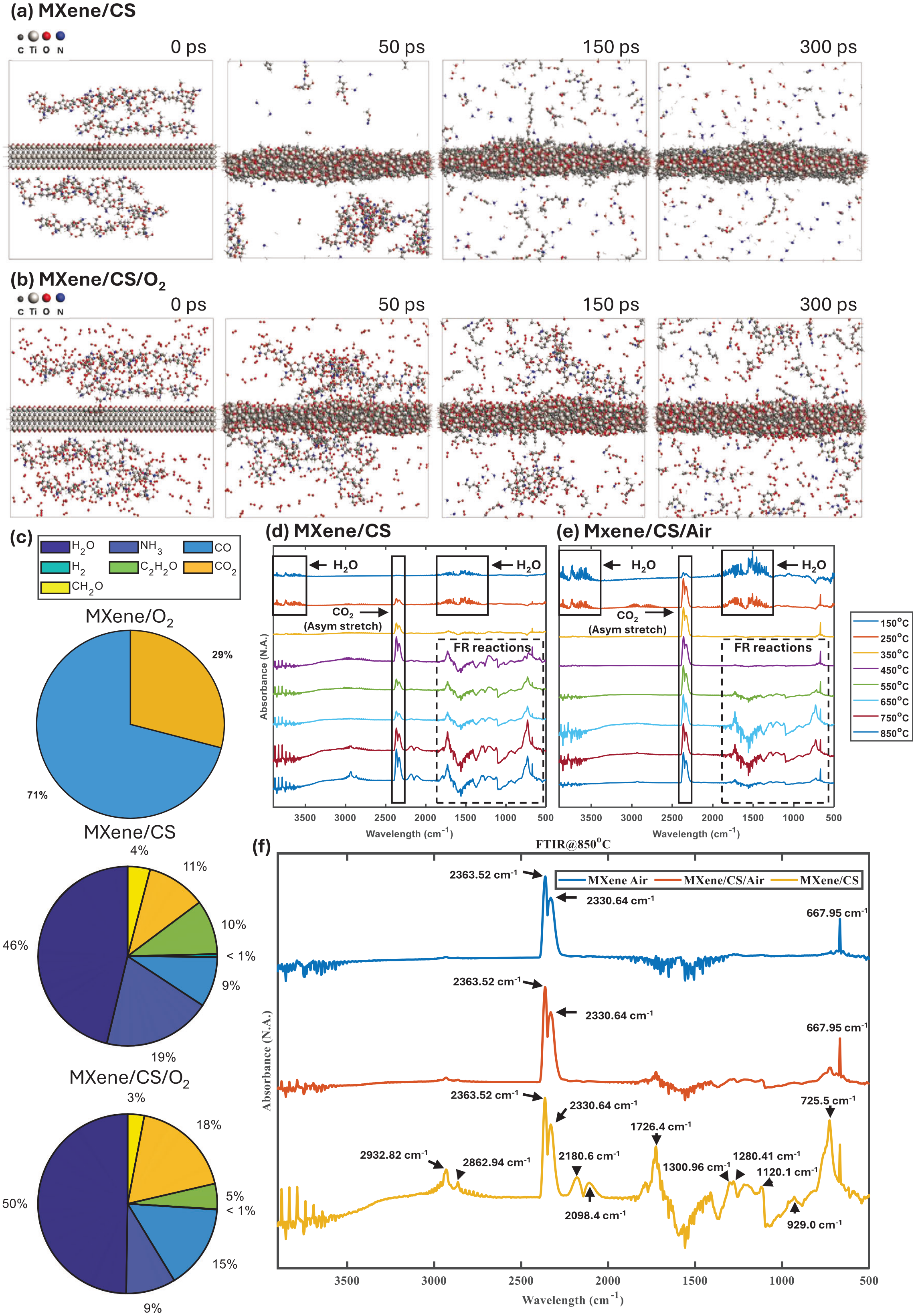

Fig. 3 | Gas-phase interactions of MXene/CS nanosheets. **a** Snapshots of MXene/CS at 3000 K; **b** Snapshots of MXene/CS/O_2 at 3000 K; **c** Gas product distribution of MXene, MXene/CS and MXene/CS/O_2. **d** TGA-FTIR spectrum of MXene/CS in nitrogen; **e** TG-IR spectrum of MXene/CS in air; **f** Comparison of TG-IR spectrum at 850°C between MXene@Air, MXene/CS@Air and MXene/CS.

(C = O stretching in carboxyl (-COOH) group)[26], 2330.64 cm^{-1} and 2363.52 cm^{-1} (C = O/C ≡ N stretching). These peaks indicate the presence of acetic acid or nitride carboxyl-based compounds decomposed from the pyranose ring. In the FR mechanism, acetic acid serves as an effective catalyst for promoting carbonisation, while nitrides eventually form ammonia and other nitrogen-containing volatiles, excluding oxygen from the system. This aligns with the large amounts of water and ammonia detected in the MD simulations.

(2) *Pyrrodine/lactam/pyridine-based*: Additional peaks were identified at 725.5 cm^{-1} (C–N bending in lactam group), 929 cm^{-1} and 1120 cm^{-1} (C-N stretching in amines), 1280 cm^{-1} (C-N stretching in amide linkage), 1420 cm^{-1} (C = O stretching in lactam carbonyl group), 1726 cm^{-1} (C = O stretching in lactam), 2862.94 cm^{-1} and 2932.82 cm^{-1} (C–H stretching in lactam ring)[27]. These findings suggest that the amine groups from glucosamine fragments could form lactam or pyridine-based structures via intramolecular cyclisation[28]. Similar compounds, such as pyrrolidone-4-carboxylic acid groups, have been detected during CS's thermal decomposition, where interactions between amine groups and acetic acids drive lactam and pyrrolidine cyclisation[29]. These reaction pathways contribute to acid-catalysed dehydration of the CS backbone, promoting char formation upon heating[30].

Figure 3(e) reveals the TGA-FTIR spectrum of MXene/CS at various temperatures in an oxygen-rich environment. Compared to the pyrolysed sample, MXene/CS exhibited more intense oxidation and evaporation from the outset, with stronger water vapour and CO_2 signals. However, FTIR-related peaks (from 725.5 cm^{-1} to 1726.4 cm^{-1}) were delayed and significantly weakened in the oxidation environment, appearing at 550 °C and rapidly vanishing at 850 °C. This could be attributed to the rigorous oxidation of both MXene and CS that disrupts the identified flame retarding reaction routes in a nitrogen ambient, where massive decarboxylation reactions take place at the CS backbone to hinder the deacetylation and cyclisation reactions.

Figure 3(f) provides a comprehensive comparison of the TGA-FTIR spectrum at 850 °C of MXene, MXene/CS in air and MXene/CS in nitrogen environment, including detailed absorbance peaks. The comparison of TGA curves between MXene and MXene/CS in the experiment can also be found in Supplementary Fig. 2.

Besides the gas-phase reactions, CS also enhances MXene's thermal resistance in the condensed phase. This effect can be evaluated by analysing the oxidised nanosheets in MD simulations.

Figure 4(a) reveals the transient evolution of the oxidised Ti_3C_2 nanosheets and the associated carbon arrangement during their oxidation with and without CS and oxygen. Compared to pure MXene oxidation, a greater carbon agglomeration was observed on the nanosheet surface after CS inclusion. Particularly, MXene/CS thermal decomposition in vacuum conditions preserved most of the carbon at the surface, forming a dense carbon layer likely to undergo carbonisation.

SEM images of residues post-TGA further illustrate the intrinsic charring capability of MXene. Figure 4(b–e) compares the residue of MXene and MXene/CS after TGA in a nitrogen environment. For MXene, distinct tetragonal TiO_2 structures emerged due to its intrinsic thermal transformation. In contrast, MXene/CS exhibited amorphous carbonaceous substrates beneath TiO_2, suggesting that CS underwent carbonisation during TGA, contributing to amorphous carbon formation alongside TiO_2 production. This observation is consistent with the XRD results, which showed a reduction in peak intensity for MXene/CS after TGA.

Figure 4(f) outlines the phase transformation of the Ti_3C_2 nanosheet by tracking the C-C, Ti-C and Ti-O bonds. The inclusion of CS intensified C-C and Ti-C bonding, leading to higher char yield and an increase in substrate elemental content. This suggests that the carbon derived from glucosamine components not only enhances the aromaticity of carbon substrates but also reinforces Ti-C bonding, improving MXene's thermal resistance while reducing Ti-O bonding, which hinders oxidation. In oxygen-deficient conditions, carbonisation was maximised, with abundant C-C double and triple bonds forming in the system.

Figure 4(g) illustrates the elemental distribution in oxidised MXene residues post-heating, tracking changes in the composition. CS inclusion significantly increases the carbon, hydrogen and nitrogen content of the Ti_3C_2 nanosheet while reducing oxygen. In general, higher C, H, and N levels indicate a more resilient carbon layer due to aromatic carbon formation. Additionally, elevated H and N concentrations suggest greater functionalisation from CS, contributing to reduced oxidation of MXene.

Figure 4(h) compares the XRD patterns of the pure MXene and MXene/CS before TGA. For pure MXene, characteristic peaks at 2θ values of around 5.8°, 17.6°, 29.7°, 35.9° and 42.2° correspond to the MXene lattice planes of (002), (004), (006), (103) and (105), respectively[31]. In MXene/CS, a distinct peak at 2θ values of around 5.6° was observed, indicating greater nanosheet layer spacing than pure MXene, likely due to CS incorporation. Moreover, the fading of peaks associated with planes (004), (006), (103), and (105) in the MXene/CS curve can also be attributed to the presence of CS, suggesting that its interfacial interactions influence MXene's crystal structure.

Post-TGA and XRD analysis (Fig. 4(i)) confirmed that both pure MXene and MXene/CS formed rutile TiO_2 as the dominant crystalline phase. Peaks at the 2θ values of 27.5°, 36.1°, 39.2°. 41.3°, 44.1°, 54.4°, and 56.7° for the MXene sample correspond to TiO_2 rutile lattice planes of (110), (101), (200), (111), (210), (211), and (220), respectively[31]. For the MXene/CS sample, these crystal planes are found at 2θ values of 27.4°, 35.9°, 39.1°, 41.1°, 43.9°, 54.2°, and 56.4°, respectively. MXene/CS displayed similar features at slightly shifted 2θ values (~27.4°–56.4°), suggesting subtle lattice structure modifications due to CS incorporation. During heating, decomposed CS provided additional elements, facilitating stable rutile TiO_2 formation, aligning with the MD simulations. Moreover, CS degradation led to amorphous carbon formation, which subsequently interacted with rutile TiO_2, slightly expanding interlayer spacing in MXene/CS, as visualised in SEM images.

Moreover, Supplementary Figs. 3–7 analyses the XPS spectrum of MXene and MXene/CS before and after TGA, where compact Ti-C-Ti and C-Ti-O characteristics were identified on the MXene/CS surface, including surface C = O and C-N groups offered by the CS. It is suggested that the CS fragments partially remain in the condensed phase in the MXene/CS residue after TG.

Interfacial/Interlayer reaction on different active sites

In the actual experiment, the deposition of Ti_3C_2/CS nanoflakes is random and misaligned, introducing uncertainties in oxidation behaviour due to varying active sites. The arbitrary orientation of nanoflakes can be examined via SEM, as shown in Supplementary Fig. 1. During thermal oxidation, the oxidation rate of Ti_3C_2 sheets and oxide expansion vary depending on crystal planes, influenced by differences in atomic coordination and the presence of diffusion channels between neighbouring MXene layers[21]. Consequently, the flame retardancy of MXene/CS sheets is also crystal plane-dependent, where molecular mobility and carbon transformation differ.

Figure 5(a), (b) illustrate the oxidation of bilayer MXene/CS with respect to (001) and (010) planes, both subjected to a temperature of 3000 K for 300 ps (see Supplementary Movie 4 and Supplementary Movie 5). For oxidation at (001) planes, MXene/CS exhibited similar oxidation and TiO_2 phase transformation as observed previously, with oxidation occurring uniformly across the outward surface of Ti_3C_2. CS reinforced the nanosheets by providing the carbon content. Notably, CS decomposed violently within the lattice, causing outward expansion of the nanosheets. On the other hand, the existing channel at the (010) plane facilitated oxygen diffusion, allowing oxidation to preferentially occur near the channel. This led to inward oxidation, reducing channel width. However, the channel also enabled CS and its decomposition products (e.g., H_2O, NH_3) to diffuse outward, limiting interaction between CS-released carbonaceous groups and MXene.

Figure 5 (c) compares the product spectrum between oxidation at two planes. Generally, fewer species were detected in both cases compared to

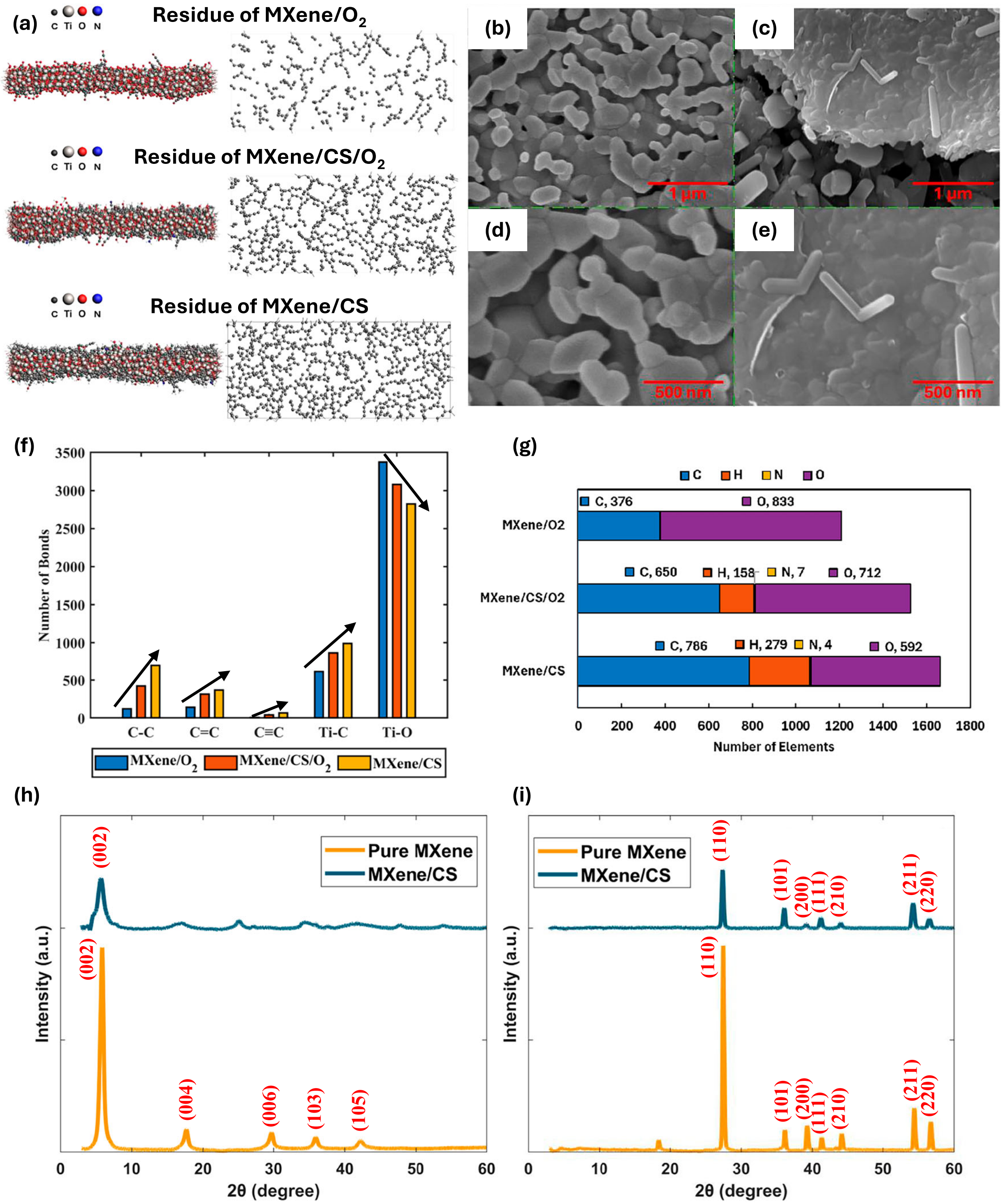

Fig. 4 | Condensed-phase interactions of MXene/CS nanosheets. **a** Residue snapshots of MXene/CS, MXene/CS/O_2 and MXene/O_2; SEM images of residues after TG (N_2) at 1 µm **b** MXene; **c** MXene/CS; and at 0.5 µm **d** MXene **e** MXene/CS. **f** Amount of carbon and titanium bonding; **g** Residue element distribution of MXene/CS, MXene/CS/O_2 and MXene/O_2; XRD spectrum of MXene and MXene/CS. **h** before TG (N_2); **i** after TG (N_2).

single-layer Ti_3C_2 systems, since bilayer configurations limit oxygen diffusion. However, the open channel at the (010) plane allowed oxygen ingress, enabling CS to oxidise and leave within the channel, hindering carbon transfer from CS to Ti_3C_2 and reducing the MXene's barrier effect.

Figure 5(d) further quantifies the number of surface functional groups on MXene, revealing the oxidation rate at different active sites: -O and -OH adsorption rates at the (010) plane were significantly higher than at the (001) plane, attributed to rapid TiO_2 formation on inward planes, where crystalline TiO_2 with O and OH termination was generated; and C adsorption was found to be more prominent at (001), where Ti_3C_2 restricted oxygen diffusion, promoting carbon agglomeration within the channel.

Figure 5(e) highlights the contribution of CS towards MXene, showcasing the residue at 300 ps and the normalised RDF spectrum of C-C pairs in different active sites. In both cases, CS significantly increased carbon deposition on MXene's inward surfaces, reducing the average C-C pair distance from 3.04 Å to 1.2 Å and 1.42 Å, indicating the formation of compact aliphatic and aromatic carbon structures. The carbonised layer is desirable for FR applications, as it safeguards against intense flames in the condensed phase. The results indicate that the MXene/CS system exhibits stronger charring ability and restricted oxygen diffusion owing to the closed surface at the (001) plane. While the (010) surfaces allow oxygen ingress via open channel, which hinders the carbonisation effect between MXene and CS. The study of flame retardancy at materials' various active sites was barely discussed and compared. This information shall provide a more in-depth understanding for future FR design, especially when the material's oxidation behaviour is sensitive towards active sites.

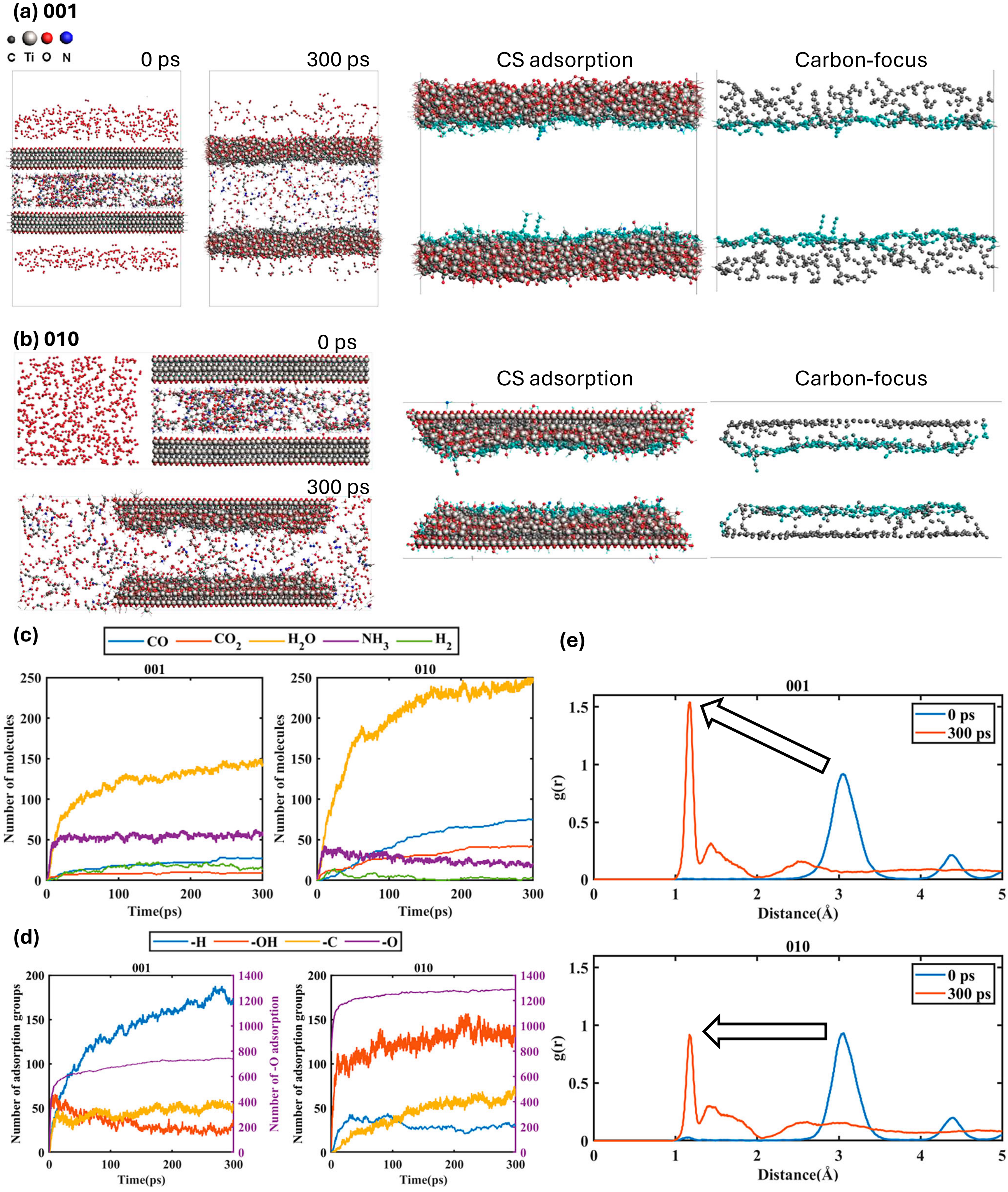

Fig. 5 | MXene/CS oxidation at various planes. a Snapshots of bilayer MXene/CS at (001) plane; **b** Snapshots of bilayer MXene/CS at (010) plane. **c** Product Distribution of bilayer MXene/CS at (001) and (010); **d** Number of adsorption groups of MXene/CS at (001) and (010); **e** Residue snapshots of case (001) and (010) with normalised RDF spectrum of CC pairs.

The flame-retardant pathway of multilayer MXene/CS

Incorporating disoriented Ti_3C_2 nanosheets with CS as a coating can ultimately facilitate the construction of a multilayer MXene/CS architecture over the material surface. Specifically, employing advanced deposition methods, such as LbL assembly, can promote uniform layering of Ti_3C_2 nanosheets and CS by leveraging charge differences during deposition. Supported by the MXene/CS interactions identified in the previous section, this section provides comprehensive insights into the flame-retarding pathway of multilayer MXene/CS systems.

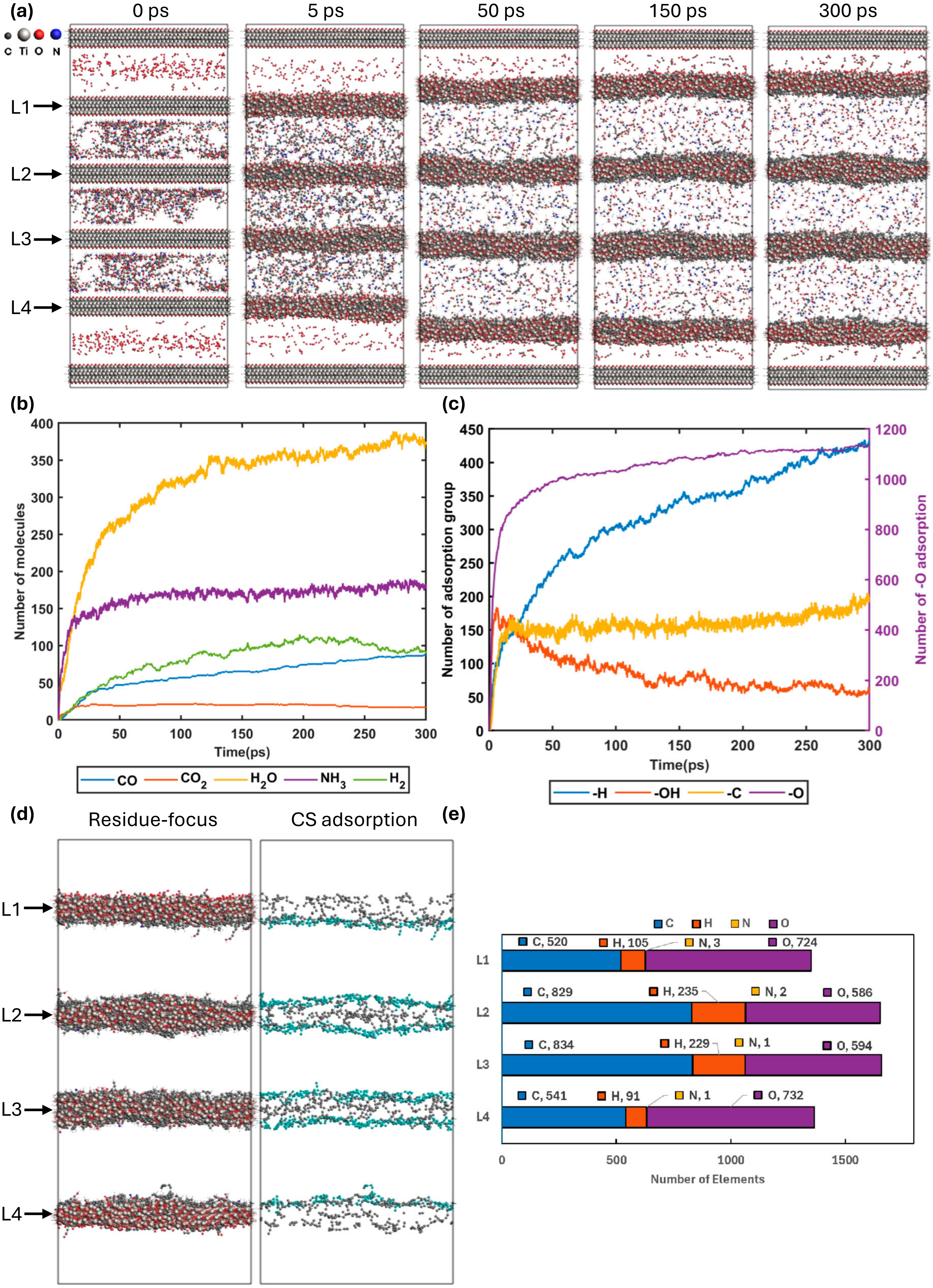

Fig. 6 | The thermal oxidation of multilayer MXene/CS nanosheets. a Snapshots of 3-bilayer MXene/CS at 3000 K; **b** Product distribution of 3-bilayer MXene/CS at 3000 K; **c** Number of adsorption group of MXene layers; **d** Schematic of the residue layers of MXene/CS; **e** Residue element distribution of each residue layer.

Figure 6(a) represents the transient evolution of a 3-bilayer MXene/CS system heated at 3000 K for 300 ps (see Supplementary Movie 6). For clarity, the MXene layers are labelled L1, L2, L3, and L4 from top to bottom. During heating, intense oxygen diffusion is observed at the surface of the exterior layers (i.e. L1 and L4), triggering outward oxide growth and transformation into rutile TiO_2. Meanwhile, CS chains in the interlayers decompose rapidly into organic volatiles (e.g., H_2O, NH_3) and aliphatic carbon fragments, as shown in Fig. 6(b). These volatiles originate from the decomposition of acetic acid-based and lactam-based compounds, resulting in acid-catalysed dehydration of the CS backbone during heating and subsequent char formation[30]. Additionally, these non-flammable organic volatiles (e.g. H_2O, NH_3) function as blowing agents, increasing char volume[32]. Furthermore, the diffusion and collision of volatile molecules significantly expand the interlayer spacing between MXene slabs.

Figure 6(c) illustrates the adsorption groups detected on the MXene surface. A rapid increase in surface oxygen (-O), hydroxyl (-OH), and hydrogen (-H) groups indicates intense oxidation throughout the system, as MXene nanosheets transform into TiO_2 via crystalline Ti-O bond formation. Meanwhile, amorphous carbon retains active sites that further adsorb -O, -OH, and -H groups via chemisorption. Surface carbon (-C) adsorption is attributed to the charring effect of CS, where CS backbone chains break down into carboxylic acid and aliphatic carbon fragments, which then crosslink or agglomerate within the MXene carbon layer. This process reinforces MXene's thermal stability.

To gain deeper insights into the charring ability of each nanosheet, Fig. 6(d) depicts the MXene nanosheet post-heating (3000 K for 300 ps). Comparatively, L2 and L3 layers retained more carbon atoms and formed denser carbon structures than the surface layers (i.e. L1 and L4). This can be attributed to the surface adsorption of carbon from CS backbones, which facilitated C–C bond formation within the amorphous carbon layer.

Figure 6(e) describes the element ratio of each MXene sheet after heating. L2 and L3 contained ~60% more carbon than the surface layers, while exhibiting 20% less oxygen, indicating higher carbonisation rates, which effectively impeded overall oxidation of the slabs. Moreover, the deposition of hydroxyl and carbon groups may terminate active sites, further preventing excessive oxidation of MXene.

During the actual experiment, the product volatiles generated during thermal decomposition could exit the layers due to misaligned coating deposition or nanosheet defects that allow volatile diffusion. Hence, periodic removal techniques were also introduced to the MXene/CS system to facilitate a more realistic gasification over the nanosheet surface; the details can be found in Supplementary Figs. 8–9.

The flame-retarding behaviour of multilayer MXene/CS coatings is anisotropic and sequential, progressing through distinct phases (see Fig. 7), which can thus be summarised as follows:

1. *Initial Oxidation at Surface Layers*: Upon exposure to heat, the surface MXene layers (i.e. L1, L4) initiate oxidation by absorbing oxygen radicals, explaining the slight weight increase observed during TGA at 400 °C (see Supplementary Fig. 2).
2. *Formation of Sacrificial TiO_2 layer*: The surface MXene layers undergo rapid oxidation, consuming surrounding oxygen. Despite the vertical heat conduction, these layers serve as sacrificial barriers, transforming into carbon-supported TiO_2, which limits oxygen diffusion deeper into the system. Additionally, TiO_2 layers exhibit excellent flame resistance, maintaining structural integrity under extreme heat (3000 K) due to compact C-C and Ti-Ti interatomic distances, which dissipate heat and restrain oxidation.
3. *CS Decomposition in Interlayers*: Within interlayers, CS undergoes dehydration reactions at low temperatures, leading to backbone monomer breakdown into carboxylic-, pyranose-, or amine-based compounds. These compounds fortify adjacent MXene layers before the sacrificial layer is depleted.
4. *Surface Adsorption and Carbon Catalysis*: Carboxylic and acid-based compounds catalyse amorphous carbon formation via surface adsorption and dehydration, enhancing thermal stability.
5. *Pyranose- and Amine-Based Compounds*: These compounds undergo ring-opening reactions, releasing NH_3, along with carboxylic and aliphatic hydrocarbons, contributing to the formation of protective carbon layers.
6. *Reinforcement* via *Ti-O-C and Ti-C-C Networks*: CS degradation reinforces adjacent MXene layers, establishing a Ti-O-C or Ti-C-C network, which hinders further oxidation.
7. *Increased Carbon Content and Structural Stability*: The formation of aromatic carbon layers elevates carbon content, correlating with char yield and thermal stability. Crosslinking with amine groups may further terminate reactive sites, slowing oxidation. XPS elemental analysis (see Supplementary Fig. 7) confirms a significant increase in carbon and nitrogen content on MXene's surface.
8. *Final Decomposition and Gas Evolution*: As the multilayer system continues flame resistance, remaining CS compounds decompose into inert volatiles (e.g. H_2O, NH_3, H_2, HNCO), which exclude oxidisers and enhance char formation.

Conclusion

This study integrates MD-ReaxFF simulations with multiscale experiments to unravel the flame-retardant behaviour of Ti_3C_2 MXene/CS hybrid nanosheets. The oxidation and decomposition pathways of MXene/CS were systematically resolved from single-slab to multilayer configurations, bridging atomic-scale reactions with macroscopic flame-retardant performance. MD simulations revealed that pristine MXene undergoes sequential Ti–C bond dissociation and TiO_2 formation, while CS incorporation fundamentally alters the oxidation chemistry by generating NH_3 and H_2O volatiles that dilute oxidisers and by depositing carbon- and nitrogen-rich residues that reinforce char formation. Under oxygen-deficient conditions, CS enhances aromatic carbonisation and intensifies C–C and Ti–C bonding, thereby suppressing oxygen diffusion and delaying degradation. Multilayer MXene/CS coatings exhibit a hierarchical defence mechanism: sacrificial TiO_2 surface layers restrict oxygen ingress, interlayer carbonisation fortifies the condensed phase, and volatile evolution sustains structural stability. These coupled gas- and condensed-phase processes establish a comprehensive mechanistic framework explaining the superior thermal resistance of MXene/CS systems. The results demonstrate that bio-derived CS not only enhances MXene's oxidation resistance but also acts as a sustainable charring and functionalising agent, offering design principles for next-generation lightweight, multifunctional flame-retardant coatings.

Numerical methods

ReaxFF simulations

The fundamentals of MD-ReaxFF revolve around the atomic movement based on Newton's second law, where F is the interatomic force, m is the atom mass, and a is the acceleration. The atomic force is contributed by the energy functions E governed by the reactive forcefield based on the correlation between bond length, bond order, and bond energy. Hence, the atoms' coordinates and velocity can be computed iteratively in the domain with the following equations:

$$\sum F = ma = m\frac{dv}{dt} = m\frac{d^2x}{dt^2} \tag{1}$$

$$F = -\nabla E \tag{2}$$

The energy parameters in the reactive forcefields were trained and validated against a wide range of experiments, QM data and DFT calculations of reaction energy and transition state of different elements. Given the potential energy of the system E_{system} which can be correlated by various interatomic energies, including bonded and non-bonded, the total energy of the system is expressed in the following:

$$E_{system} = \underbrace{E_{bond} + E_{over} + E_{under} + E_{val} + E_{pen} + E_{tors} + E_{conj}}_{Bonded\ Energy} + \underbrace{E_{vdWaals} + E_{Coulomb}}_{Non-bonded\ Energy} \tag{3}$$

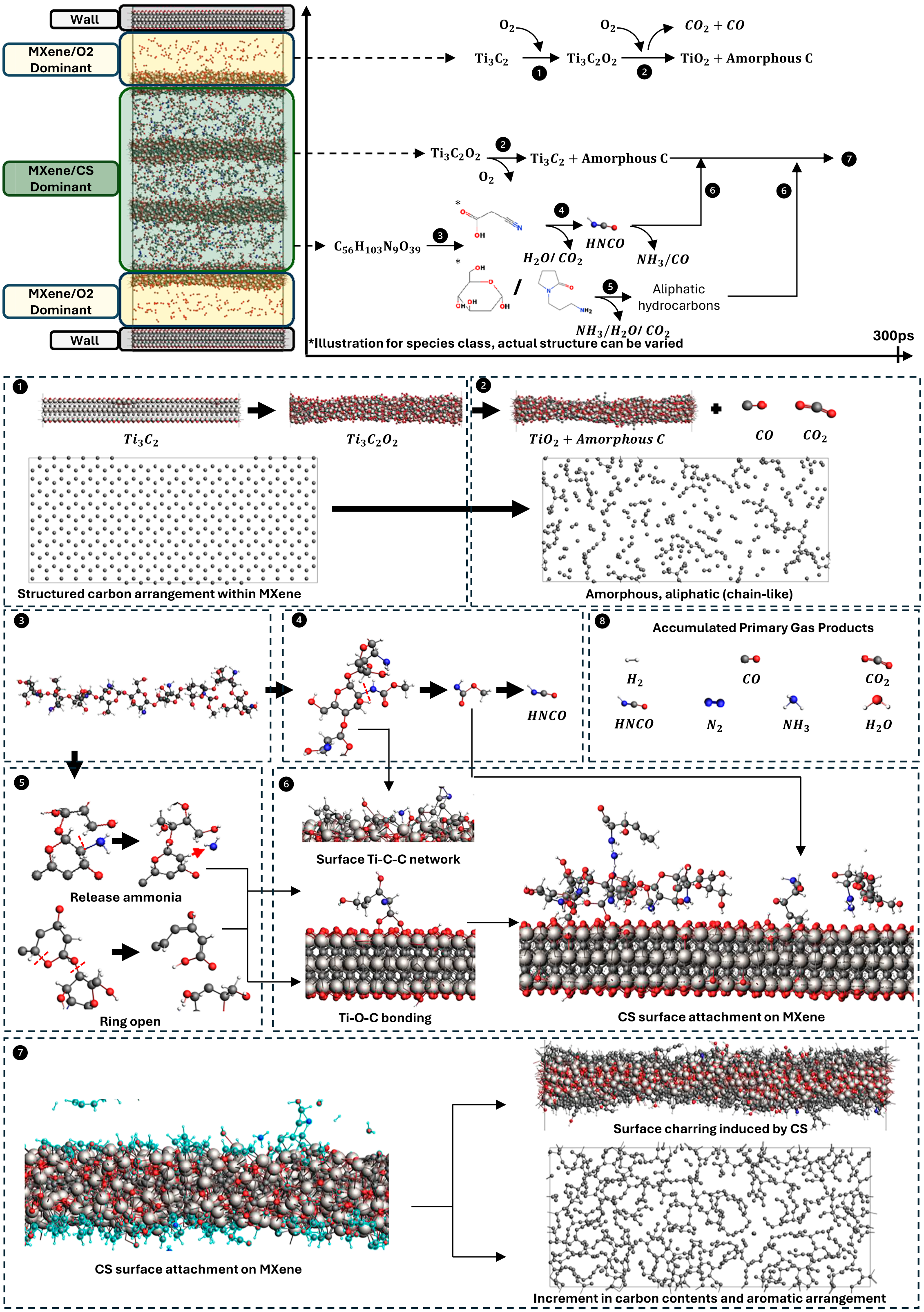

Fig. 7 | Summarised flame retarding pathway of multilayer MXene/CS. Schematics illustrating the flame retardant reactions at different layers, including both reaction pathways and morphological changes.

where E_{bond} denotes the bond energy based on interatomic distance, E_{over} and E_{udner} are the over-coordinated and under-coordinated atoms in the bond energy calculation. E_{val}, E_{pen}, E_{tors}, E_{conj} represent the complex consideration of various atomic forces, including valence angle term, penalty and torsion energy, and conjugation effects. While $E_{vdWaals}$, $E_{coulomb}$ represent non-bonded interactions such as Van der Waals and Coulomb interaction. Furthermore, the bond order was evaluated based on the interatomic distance between each atom in the domain in every

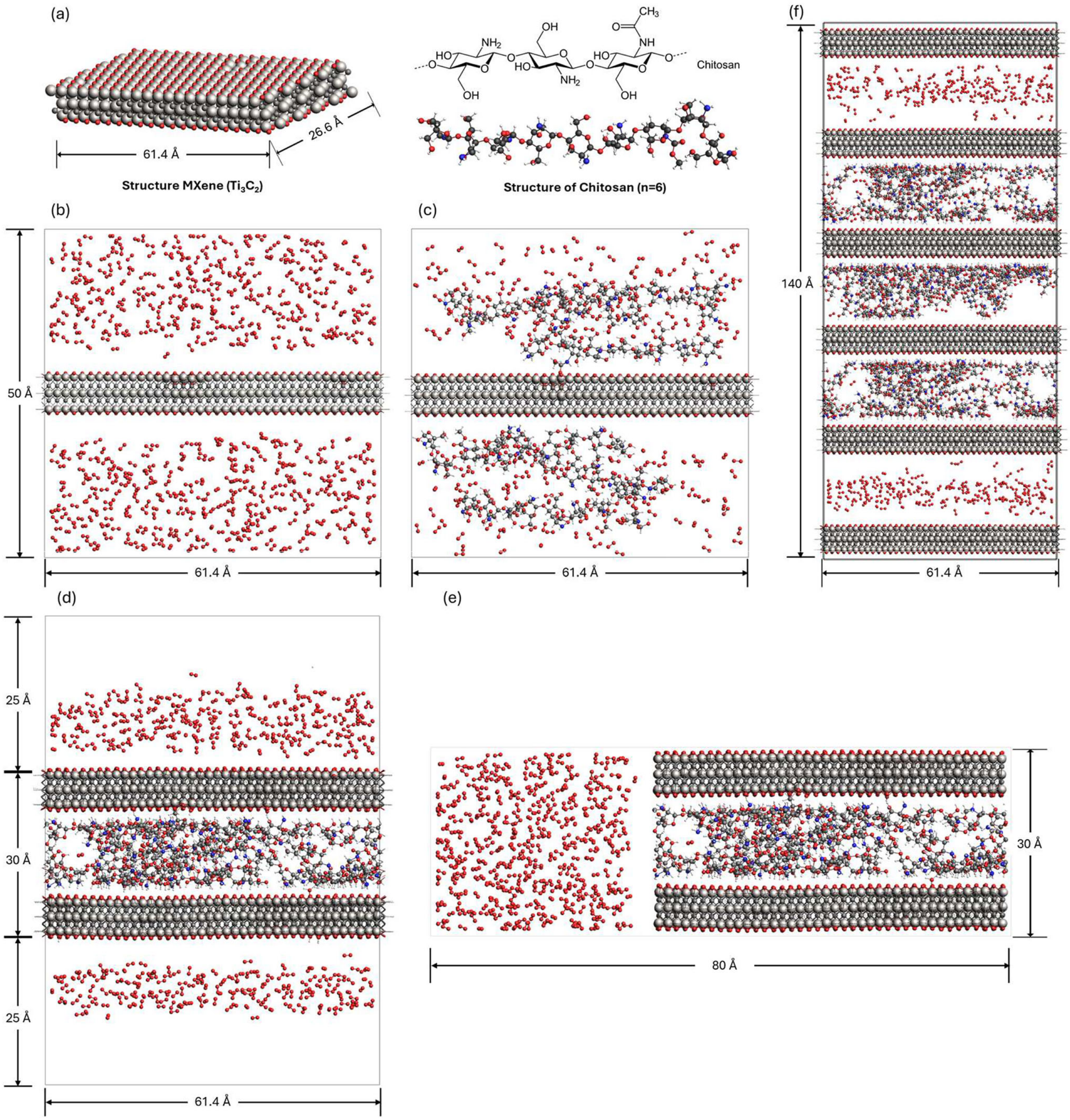

Fig. 8 | Molecular geometry of MXene/CS nanosheets. a The molecule unit of MXene and CS; **b** The molecular geometry of MXene/O_2; **c** MXene/CS/O_2; **d** MXene/CS bilayer with respects to (001) oxidation; **e** MXene/CS bilayer with respect to (010) oxidation; **e** Stack MXene/CS layer.

timestep, adopting the empirical formula[33,34] in Eq. (4):

$$\mathrm{BO_{ij}} = BO_{ij}^{\sigma} + BO_{ij}^{\pi} + BO_{ij}^{\pi\pi} = \exp\left[p_{bo1}\left(\frac{r_{ij}}{r_0^{\sigma}}\right)^{p_{bo2}}\right] + \exp\left[p_{bo3}\left(\frac{r_{ij}}{r_0^{\pi}}\right)^{p_{bo4}}\right] + \exp\left[p_{bo1}\left(\frac{r_{ij}}{r_0^{\pi\pi}}\right)^{p_{bo6}}\right] \tag{4}$$

where $\mathrm{BO_{ij}}$ is the bond order between atoms i and j, r_{ij} denotes the distance between atoms and r_0 are the equilibrium bond length for bonds σ, π and $\pi\pi$. Following an initial calculation of bond orders, a correction procedure is implemented to account for over-coordination and valence angles. This correction step is crucial in achieving the appropriate long-range orders for odd-electron radical molecules and short-range localised orders for even-electron stable molecules[35].

Simulation setup

The computational chemistry framework employed in this study aims to characterise the thermal oxidative behaviour of MXene nanosheets and their interactions with CS under different layering configurations. To achieve this, a series of MD-ReaxFF simulations were conducted on Ti_3C_2 MXene slabs, both with and without CS, as well as in the presence and absence of adjacent oxygen molecules. Firstly, a single Ti_3C_2 lattice (see Fig. 8(a)) terminated with oxygen (600 Ti, 400 C and 400 O) was created in the domain at 61.41 Å x 26.59 Å x 50 Å. The oxygen molecules and CS ($n = 6$) (see Fig. 8(b), (c)) were inserted into spatial regions via PACKMOL[36].

It is worth noting that MXene/CS geometry in the absence of oxygen is also investigated in the results section. The constructed single-slab geometry enables perspicuous exploration of the intrinsic oxidation of MXene and the surface reactions with CS and oxygen molecules. Afterwards, a two-layer/bilayer configuration (see Fig. 8(d), (e)) is proposed to study the interlayer interactions and the plane-dependent FR behaviour of the MXene/CS bilayer. Ultimately, as shown in Fig. 8(f), a multilayer architecture consisting of 3 MXene/CS bilayers is developed to reveal the FR strategies of engineered layers. It is notable that the Ti_3C_2 slabs next to z-edges are fixed to act as a "wall". The non-reactive "wall" can effectively prevent numerical instability caused by high-velocity gradients at the periodic boundaries.

All simulations were initiated with a heating-up process with a time step of 0.1 fs, followed by the NVT ensemble, where the temperature was regulated using the Berendsen thermostat. Firstly, the temperature of the models would ramp up from 300 K to T_{max} (2000 K, 2500 K and 3000 K) at the first 50 ps, which enables continuous reactions during the temperature being elevated from the ambient[37], reactions with different energy barriers (i.e., surface diffusion or functionalisation) were characterised transiently to outline the pyrolysis stages. Afterwards, the temperature was maintained at T_{max} for another 250 ps under NVT ensemble to accelerate the oxidation of the system. The artificial temperature range was adopted to observe the thermal decomposition, as the artificial heat can promote sufficient atomic motion and molecular collision with practical computational cost[38,39]. In previous MD-ReaxFF studies on MXene oxidation, 3000 K was adopted to observe the full MXene oxidation reaction[19]. This simulation strategy was adopted and validated by various ReaxFF literature[40,41]. All the simulations in this study were carried out in Amsterdam Modelling Suite (AMS)[42]. The details of the ReaxFF forcefield used in this study are provided in Supplementary Note. 1.

Experimental characterisation

Raw materials

Titanium aluminium carbide (Ti_3AlC_2) was obtained from the 11 Technology Co. Ltd. (Changchun, China). Chitosan (CS, Mw. 1,500,000), hydrochloric acid (HCl, 36% aq.) and lithium fluoride (LiF) were supplied by Sigma-Aldrich.

Sample preparation

MXene (Ti_3C_2) nanosheet suspension was fabricated with a concentration of 1 mg/mL based on previous work carried out by Lin et al.[11]. Chitosan solution was prepared by dissolving the chitosan powder in the deionised (DI) water to form a 0.5 wt.% solution. Diluted HCl was added to the chitosan solution at the same time to maintain a pH value of 5 during the dissolving process. Pure MXene sample was obtained by suction filtration of the nanosheet suspension, followed by vacuum drying. To prepare the FR coating, the MXene suspension was mixed with the CS solution at a ratio of 3.26 to align with the numerical model. After that, the mixture was fast-frozen by liquid nitrogen, and then dried by the freeze-drying method to acquire the final samples for further characterisation. The fabricated samples are named MXene and MXene/CS (MXene to chitosan ratio of 3.26).

Characterisation

Thermogravimetric analysis (TGA) equipped with Fourier Transform Infrared Spectroscopy (FTIR) was adopted to understand the thermal degradation process of the samples on Netzsch TG 209 F1 thermogravimetry equipment. The heating rate was 20 K/min with a temperature range from ambient temperature to 900˚C under both nitrogen and air atmospheres. Scanning electron microscopy (SEM) on a Hitachi SU8010 SEM (Tokyo, Japan) with the acceleration voltage of 10 kV was applied to observe the surface morphology of the samples for both before and after the TGA examination. The samples were coated with platinum prior to the SEM testing to prevent charging effects during imaging. X-ray diffraction (XRD) patterns were recorded on an XRD-Empyrean I (Cu power) with the CuKα wavelength of 1.54 Å. X-ray photoelectron spectroscopy (XPS) was conducted on Thermo ESCALAB250i XPS (Thermo Scientific, UK) with a mono-chromated AlKα excitation energy of 1486.68 eV and a binding energy reference of C1s = 284.8 eV for adventitious hydrocarbon.

Data availability

All experiment and numerical data are available in the main text or the supplementary materials, and are also available from the corresponding author on reasonable request. Request or enquiry can be made by contacting: anthony-cy.yuen@polyu.edu.hk.

Received: 2 July 2025; Accepted: 16 October 2025;

References

1. Lazar, S. T., Kolibaba, T. J. & Grunlan, J. C. Flame-retardant surface treatments. *Nat. Rev. Mater.* **5**, 259–275 (2020).
2. G. H. Yeoh, et al., "Carbon-based flame retardants for polymers: a bottom-up review," *Adv. Mater*. **36**, 2403835, (2024).
3. Naguib, M. et al. "Two-dimensional nanocrystals produced by exfoliation of Ti3AlC2,". *Adv. Mater.* **23**, 4248–4253 (2011).
4. Lin, B. et al. MXene based flame retardant and electrically conductive polymer coatings. *Polymers* **16**, 2461 (2024).
5. Singh, M. & Singh, A. K. "Performance improvement of photovoltaic: utilization of two-dimensional Ti3C2Tx MXene,. *Surf. Interfaces* **27**, 101566 (2021).
6. Li, Z. et al. Synthesis and thermal stability of two-dimensional carbide MXene Ti3C2. *Mater. Sci. Eng.: B* **191**, 33–40 (2015).
7. Naguib, M. et al. "One-step synthesis of nanocrystalline transition metal oxides on thin sheets of disordered graphitic carbon by oxidation of MXenes. *Chem. Commun.* **50**, 7420–7423 (2014).
8. K. Gong and K. Zhou, "Flame-retardant properties of MXene-based polymer nanocomposites," in *Flame Retardant Nanocomposites,* pp. 287-320 (Elsevier, 2024).
9. C. Yang, et al., Layer-by-layer assembled aramid nanofiber/MXene aerogel: exceptional resistance to extreme temperatures and robust anisotropy for advanced applications. *Compos. Sci. Technol.* **257**, 110833 (2024).
10. Lin, B. et al. Experimental and numerical perspective on the fire performance of MXene/Chitosan/Phytic acid coated flexible polyurethane foam. *Sci. Rep.* **11**, 4684 (2021).
11. Lin, B. et al. MXene/chitosan nanocoating for flexible polyurethane foam towards remarkable fire hazards reductions. *J. Hazard. Mater.* **381**, 120952 (2020).
12. Liu, F. et al. Well-aligned MXene/chitosan films with humidity response for high-performance electromagnetic interference shielding. *Carbohydr. Polym.* **243**, 116467 (2020).
13. Wang, B. et al. Multifunctional MXene/chitosan-coated cotton fabric for intelligent fire protection. *ACS Appl. Mater. Interfaces* **13**, 23020–23029 (2021).
14. A. K. Rana, V. K. Gupta, P. Hart, F. Scarpa, and V. K. Thakur. Sustainable MXene-chitosan/chitin composites for Interdisciplinary applications in water purification, bio-medical, bio-sensing and electronic fields. *Mater. Today Sustain.* **25**, 100671 (2024).
15. P. Zheng, et al. The eruption of carbon chains in the oxidation of 2D Tin + 1Cn (n= 1, 2, 3) MXenes," *Appl. Surf. Sci.* **550**, 149310 (2021).
16. Berdiyorov, G. R. & Mahmoud, K. A. Effect of surface termination on ion intercalation selectivity of bilayer Ti3C2T2 (T= F, O and OH) MXene. *Appl. Surf. Sci.* **416**, 725–730 (2017).
17. Plummer, G., Anasori, B., Gogotsi, Y. & Tucker, G. J. Nanoindentation of monolayer Tin+ 1CnTx MXenes via atomistic simulations: the role of composition and defects on strength. *Comput. Mater. Sci.* **157**, 168–174 (2019).
18. van Duin, A. C. T., Dasgupta, S., Lorant, F. & Goddard, W. A. ReaxFF: a reactive force field for hydrocarbons. *J. Phys. Chem. A* **105**, 9396–9409 (2001).
19. Lotfi, R., Naguib, M., Yilmaz, D. E., Nanda, J. & Van Duin, A. C. A comparative study on the oxidation of two-dimensional Ti 3 C 2 MXene structures in different environments. *J. Mater. Chem. A* **6**, 12733–12743 (2018).

20. Badawy, K., Liao, K. & Singh, N. Atomistic insights of Ti-based MXenes thermal decomposition and transformation to carbon-supported Ti–O phases for energy applications. *ACS Appl. Nano Mater.* **5**, 16731–16740 (2022).
21. Y. Liu, et al. The mechanism of room-temperature oxidation of a HF-etched Ti3C2T x MXene determined via environmental transmission electron microscopy and molecular dynamics. *InfoMat*, e12536 (2024).
22. Cao, Y. et al. Enhanced thermal properties of poly (vinylidene fluoride) composites with ultrathin nanosheets of MXene. *RSC Adv.* **7**, 20494–20501 (2017).
23. Natu, V. et al. A critical analysis of the X-ray photoelectron spectra of Ti3C2Tz MXenes. *Matter* **4**, 1224–1251 (2021).
24. Laufer, G., Kirkland, C., Cain, A. A. & Grunlan, J. C. Clay–chitosan nanobrick walls: completely renewable gas barrier and flame-retardant nanocoatings. *ACS Appl. Mater. interfaces* **4**, 1643–1649 (2012).
25. Ou, C. et al. Study on the thermal degradation kinetics and pyrolysis characteristics of chitosan-Zn complex. *J. Anal. Appl. Pyrolysis* **122**, 268–276 (2016).
26. Jiao, C., Li, M., Chen, X. & Li, S. Flame retardancy and thermal decomposition behavior of TPU/chitosan composites. *Polym. Adv. Technol.* **31**, 178–188 (2020).
27. Linstrom, P. J. & Mallard, W. G. The NIST Chemistry WebBook: A chemical data resource on the internet. *J. Chem. Eng. Data* **46**, 1059–1063 (2001).
28. Chen, J. & Ho, C.-T. Volatile compounds formed from thermal degradation of glucosamine in a dry system. *J. Agric. Food Chem.* **46**, 1971–1974 (1998).
29. Sirvio, J. A., Kantola, A. M., Komulainen, S. & Filonenko, S. Aqueous modification of chitosan with itaconic acid to produce strong oxygen barrier film. *Biomacromolecules* **22**, 2119–2128 (2021).
30. Wu, X., Yang, C. Q. & He, Q. Flame retardant finishing of cotton fleece: part VII. Polycarboxylic acids with different numbers of functional group. *Cellulose* **17**, 859–870 (2010).
31. Alothman, A. A. et al. Ti3C2-MXene/NiO nanocomposites-decorated CsPbI3 perovskite active materials under UV-light irradiation for the enhancement of crystal-violet dye photodegradation. *Nanomaterials* **13**, 3026 (2023).
32. Ren, Y., Tian, T., Jiang, L. & Guo, Y. Fabrication of chitosan-based intumescent flame retardant coating for improving flame retardancy of polyacrylonitrile fabric. *Molecules* **24**, 3749 (2019).
33. Van Duin, A. C., Dasgupta, S., Lorant, F. & Goddard, W. A. ReaxFF: a reactive force field for hydrocarbons. *J. Phys. Chem. A* **105**, 9396–9409 (2001).
34. Senftle, T. P. et al. The ReaxFF reactive force-field: development, applications and future directions. *npj Comput. Mater.* **2**, 1–14 (2016).
35. Liang, T. et al. Reactive potentials for advanced atomistic simulations. *Annu. Rev. Mater. Res.* **43**, 109–129 (2013).
36. Martínez, L., Andrade, R., Birgin, E. G. & Martínez, J. M. PACKMOL: a package for building initial configurations for molecular dynamics simulations. *J. Comput. Chem.* **30**, 2157–2164 (2009).
37. Li, X., Zheng, M., Ren, C. & Guo, L. ReaxFF molecular dynamics simulations of thermal reactivity of various fuels in pyrolysis and combustion. *EnergyFuels* **35**, 11707–11739 (2021).
38. So/rensen, M. R. & Voter, A. F. Temperature-accelerated dynamics for simulation of infrequent events. *J. Chem. Phys.* **112**, 9599–9606 (2000).
39. De Cachinho Cordeiro, I. M. et al. Atomistic characterisation of graphite oxidation and thermal decomposition mechanism under isothermal and Non-Isothermal heating scheme. *J. Comput. Mater. Sci.* **210**, 111458 (2022).
40. Salmon, E., van Duin, A. C., Lorant, F., Marquaire, P.-M. & Goddard, W. A. III Early maturation processes in coal. Part 2: reactive dynamics simulations using the ReaxFF reactive force field on Morwell Brown coal structures. *Org. Geochem.* **40**, 1195–1209 (2009).
41. Salmon, E., van Duin, A. C., Lorant, F., Marquaire, P.-M. & Goddard, W. A. III Thermal decomposition process in algaenan of Botryococcus braunii race L. Part 2: Molecular dynamics simulations using the ReaxFF reactive force field. *Org. Geochem.* **40**, 416–427 (2009).
42. M. F. R. Rüger, et al., "AMS 2024.1," 2024.103 ed. Vrije Universiteit, Amsterdam, The Netherlands: SCM, Theoretical Chemistry, 2024.

Acknowledgements

All financial and technical support is deeply appreciated by the authors. This research was sponsored by the Australian Research Council (ARC Discovery Project (DP220101427), ARC Research Hub for Fire Resilience Infrastructure, Assets and Safety Advancements (IH220100002) and ARC Centre of Excellence for Carbon Science and Innovation (CE230100032). This research work is also sponsored by the PolyU UGC funding (P0044994) and (P0052426). Hong Kong Research Grant Council General Research Fund/Early Career Scheme (25200925). City University of Hong Kong Internal Grant (Project No: 9610681).

Author contributions

I.M.D.C.C: Original draft, Software, Methodology, Investigation, Formal analysis, Data curation, Conceptualization. T.B.Y.: Review & editing, Methodology, Investigation, Forcefield Training, Conceptualization. A.C.Y.Y.: Supervision, Visualization, Validation, Methodology, Investigation. B.L.: Experiment, Material Synthesis, Characterization. M.J.: Writing—review and editing, Project administration. W.W.: Resources, Project administration. Q.C.: Methodology, Investigation, Formal analysis. W.Y.: Supervision, Resources, Project administration, Funding acquisition. C.T.: Resources, Project administration, Formal analysis. C.W.: Supervision, Resources, Project administration. G.H.Y.: Supervision, Resources, Project administration, Funding acquisition.

Competing interests

The authors declare no competing interests.

Additional information

Supplementary information The online version contains supplementary material available at https://doi.org/10.1038/s43246-025-00997-8.

Correspondence and requests for materials should be addressed to Anthony Chun Yin Yuen or Guan Heng Yeoh.

Peer review information *Communications Materials* thanks Sabyasachi Gaan and the other anonymous reviewer(s) for their contribution to the peer review of this work. A peer review file is available.